Interconnected effects of Sm-doping on grain structure and transport properties of the textured $Bi_{2-x}Sm_xTe_{2.7}Se_{0.3}$ compounds

Maxim Yaprintsev [a], Alexei Vasil'ev [b], Oleg Ivanov [a,b,*], Daniil Popkov [a]

[a] Belgorod State University, Belgorod, 394015, Russian Federation
[b] Belgorod State Technological University Named after V.G. Shukhov, Belgorod, 308012, Russian Federation

ARTICLE INFO

ABSTRACT

Textured $Bi_{2-x}Sm_xTe_{2.7}Se_{0.3}$ compounds with $x = 0$; 0.005; 0.01; 0.02; 0.05; 0.1; 0.2 and 0.3 were prepared by using solvothermal synthesis and spark plasma sintering of starting powders. Sm-doping results in several interconnected effects. First of them is reducing in size of particles in starting powders with increasing x. This effect is attributed to increasing in ionic bonding fraction in polar covalent Bi(Sm)-Te bonds, which occurs at increasing Sm content due to difference in electronegativity of Bi and Sm. With increasing x, grain size in bulk samples is also reducing, which is governed by relevant changing in the size of particles. This effect also results in enhancing in texturing degree in samples at gradual increasing x. Finally, grain size effects on the specific electrical resistivity and the thermal conductivity are observed in bulk samples with different grain size. With increasing the grain size, the resistivity increases, whereas the total thermal conductivity decreases. These features are due to electron scattering by grain boundaries.

1. Introduction

In accordance with the Ioffe expression, thermoelectric efficiency of material can be expressed via the thermoelectric figure-of-merit, $ZT = TS^2/\rho k$, where T is the absolute temperature, S is the Seebeck coefficient, ρ is the specific electrical resistivity and k is the total thermal conductivity with electronic and phonon contributions [1]. To maximize ZT, ρ and k, which are the transport properties of material, should be simultaneously reduced. However, reducing in ρ is usually accompanied by relevant enhancing in k, and vice versa. Optimal ρ and k tuning is key problem in thermoelectric materials science. To optimize ρ and k, specific microstructure, which includes various defects with desired properties, shape, size, dimensionality and etc., is usually formed via various approaches and ways of defect engineering [2–5]. Elemental doping is one of fruitful ways that is often applied to optimally tune the transport properties and, hence, enhance thermoelectric efficiency of material [6–15]. Dopant atoms can behave as donor or acceptor centres, resulting in reducing in ρ and enhancing in the electronic contribution to k. Besides, dopant atoms are effective scattering centres for electrons and phonons, resulting in enhancing in ρ and reducing in the phonon contribution to k, respectively. Rare earth elements, R (R = Lu, Gd, Ce, etc.), are found to be effective dopants, improving the thermoelectric

properties of Bi_2Te_3-based compounds [16–27]. Usually, the R atoms substitute for Bi in crystal Bi_2Te_3 structure. Besides direct effect of the R-doping on the thermoelectric properties, other effects accompanying this doping can be also observed. These effects can indirectly affect the thermoelectric properties, too. In particularly, owing to rather different electronegativities of the Bi and R atoms, a degree of ionicity in polar covalent Bi–Te bond, existing in crystal Bi_2Te_3 structure, increases, when a partial substitution of R for Bi takes place in this bond. As result, a size of particles in starting $Bi_{2-x}R_xTe_3$ powders, which are chemically synthesized in polar solvents, decreases with increasing R content. Mechanism of this phenomenon, which is earlier observed in $Bi_{2-x}Sm_xTe_{2.7}Se_{0.3}$ particles, was discussed in Ref. [28]. In turn, the size of particles in starting powder can affect a size of grains in relevant bulk material, prepared via consolidation and high-temperature treatment of this powder. Namely, bigger size of the particles will result in bigger size of the grains. Therefore, increasing in R content in R-doped Bi_2Te_3 compounds can be accompanied by decreasing in the grain size in these compounds. In grained thermoelectric materials, grain boundaries are specific defects, scattering electrons and phonons [29–31]. By governing the grains size, ρ and k can be additionally tuned in desired manner via grain size effects on the transport properties of grained material [32–35].

The main purpose of this paper is to analyse the Sm-doping effect on features in the specific electrical resistivity and the total thermal conductivity of textured $Bi_{2-x}Sm_xTe_{2.7}Se_{0.3}$ compounds ($x = 0$; 0.005; 0.01; 0.02; 0.05; 0.1; 0.2 and 0.3), which are originated from changing in grain structure under this doping. By changing x, samples with different grain size, which is x-dependent, were successfully prepared. Grain size effects in the specific electrical resistivity and the total thermal conductivity were then found. At present, $Bi_2Te_{2.7}Se_{0.3}$ is the best material with electronic conductivity for various low-temperature applications [36, 37]. It is known that Bi_2Te_3-based compounds, having a layered crystal structure, are readily textured via technological processes, which are based on uniaxial pressuring a starting powder [38–46]. The textured material is characterized by a preferential orientation of the grains. The texturing results in partial recovering anisotropy in the thermoelectric properties of grained material, which is inherent to relevant single crystal. The texturing allows maximizing ZT in textured Bi_2Te_3-based compounds.

2. Materials and methods

To prepare the $Bi_{2-x}Sm_xTe_{2.7}Se_{0.3}$ compounds with $x = 0$; 0.005; 0.01; 0.02; 0.05; 0.1; 0.2 and 0.3, solvothermal synthesis of starting powders and following spark plasma sintering (SPS) of these powders were applied. Analytically pure $(Bi(NO_3)_3 \cdot 5H_2O$, TeO_2, SeO_2, $Sm(NO_3)_3 \cdot 6H_2O$, NaOH, poly(1-ethenylpyrrolidin-2-one), ethane-1,2-diol) chemicals were applied to synthesize starting powders. First, $Bi(NO_3)_3 \cdot 5H_2O$, TeO_2, $Sm(NO_3)_3 \cdot 6H_2O$ were taken in a stoichiometric ratio corresponding to x and dissolved in the 90 cm^3 ethane-1,2-diol NaOH and 15 g NaOH mixture of under vigorous stirring by a magnetic stirrer. Poly(1-ethenylpyrrolidin-2-one) (Mr = 12 000), acting as solution, was then added to the reaction mixture. The mixture was again under vigorous stirring for 30 min. After, the mixture was put in an autoclave that was sealed and maintained at 190°C for 5 min. Then the autoclave was naturally cooled to room temperature. After completing the solvothermal synthesis reaction, dark grey precipitate was taken out by centrifuging and washed with deionized water and ethyl alcohol several times and then dried at 80°C for 8 h. Starting powders were spark-plasma-sintered using a SPS-25/10 system at pressure of 40 MPa and temperature of 680 K for 2.5 min in vacuum, resulting in the Ø20 mm × 15 mm cylinders.

To examine the transport properties of the $Bi_{2-x}Sm_xTe_{2.7}Se_{0.3}$ compounds, 2 × 2 × 10 mm bars and Ø10 × 2 mm disks were prepared. Bar samples were applied to measure the specific electrical resistivity by four-probe method (a ZEM-3 system), whereas disk-shaped samples were applied to measure the total thermal conductivity of by laser flash method (a TC-1200 system). A Mini Cryogen Free Measurements System (Cryogenic Ltd, UK) was applied to examine the Hall effect and estimate the concentration and Hall mobility of electrons. The Archimedes' method was applied to measure density of bulk samples. To identify crystal structure, phase composition of starting powders and bulk samples, as well as estimate a degree of grain ordering in textured samples, X-ray diffraction (XRD) analysis was performed by using a Rigaku Ultima IV diffractometer with CuK$_\alpha$-radiation. To analyse morphology of particles in starting powders, estimate average particles size and study grain structure features in bulk samples, scanning electron microscopy (SEM) was applied by using a Nova NanoSEM 450 microscope.

3. Results and discussion

3.1. Sm-doping effect on particle size in starting $Bi_{2-x}Sm_xTe_{2.7}Se_{0.3}$ powders

As resulted from XRD analysis, all the starting $Bi_{2-x}Sm_xTe_{2.7}Se_{0.3}$ powders with different x are single hexagonal $R\overline{3}m$ phase that corresponds to pure Bi_2Te_3 (PDF#01-089-4302). XRD pattern for starting
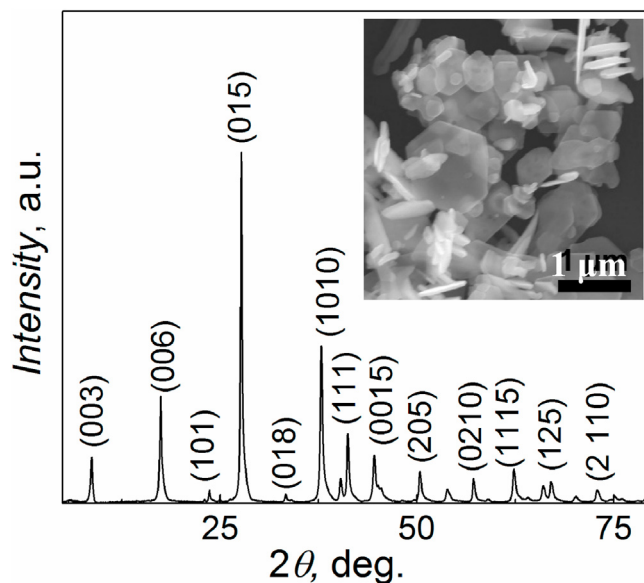

Fig. 1. XRD pattern for the starting $Bi_{1.9}Sm_{0.1}Te_{2.7}Se_{0.3}$ powder. Inset is SEM image of the particles in the same powder.

powder with $x = 0.1$ is presented in Fig. 1. Inset to Fig. 1 shows SEM image of the particles in this starting powder. According to SEM examination, all the starting powders mainly consisted of hexagonal plate-shaped particles. Hexagonal habitus of the particles corresponds to hexagonal symmetry of the $Bi_{2-x}Sm_xTe_{2.7}Se_{0.3}$ compounds. Forming the plate-shaped particles during a chemical synthesis of Bi_2Te_3-based compounds is related to specific features of crystal structure and chemical bonds of these compounds [36,37]. In accordance with results of EDX (energy dispersive X-ray spectroscopy) mapping, which was earlier reported earlier in Ref. [28], Bi, Te, Sm and Se are uniformly distributed within the particles, and, in accordance with results of SAED (selected area electron diffraction) experiment, the individual $Bi_{1.95}Sm_{0.05}Te_{2.7}Se_{0.3}$ particles in the starting powder are single-crystalline particles with crystal Bi_2Te_3 structure.

It was found that the Sm-doping remarkably affects a size of the particles in the starting $Bi_{2-x}Sm_xTe_{2.7}Se_{0.3}$ powders. To estimate average values of a lateral size, l_a, and a thickness, h_a, of the particles, histograms of the l and h distributions for the compositions with different x were plotted. All the histograms were satisfactory described by the lognormal unimodal distribution [47]. The lognormal probability density function is expressed as

$$F(l \text{ or } h) = \frac{1}{\sqrt{2\pi}\sigma l_a(\text{or } h_a)} \exp\left(-\frac{\ln(l \text{ or } h) - \ln(l_a \text{ or } h_a)^2}{2\sigma^2}\right) \quad (1)$$

where σ is the standard deviations of the logarithms of l or h. These deviations characterize a width of the relevant $F(l)$ or $F(h)$ distributions.

The $l_a(x)$ and $h_a(x)$ dependences are presented in Fig. 2 (a). With increasing Sm content, l_a remarkably decreases from ~460 nm for $x = 0$ down to ~320 nm for $x = 0.3$, whereas h_a is x-independent and equal to ~70 nm for all the compositions. For small x values ($x < 0.02$), l_a is very rapidly falling with increasing x, but for $x \geq 0.02$ l_a is falling much more slowly. Particle shape factor, l_a/h_a, can be introduced to characterize a shape of the particles in the starting $Bi_{2-x}Sm_xTe_{2.7}Se_{0.3}$ powders. The l_a/h_a versus x dependence is shown in inset to Fig. 2 (a). This dependence is governed by the $l_a(x)$ and $h_a(x)$ dependences. With increasing Sm content, l_a/h_a is non-monotonically decreasing. However, for all the compositions, $l_a/h_a \gg 1$, i.e. the particles are 2D-objects. Maximal l_a/h_a value corresponds to undoped sample, whereas minimal l_a/h_a value is observed for the composition with maximal Sm content. The standard deviations
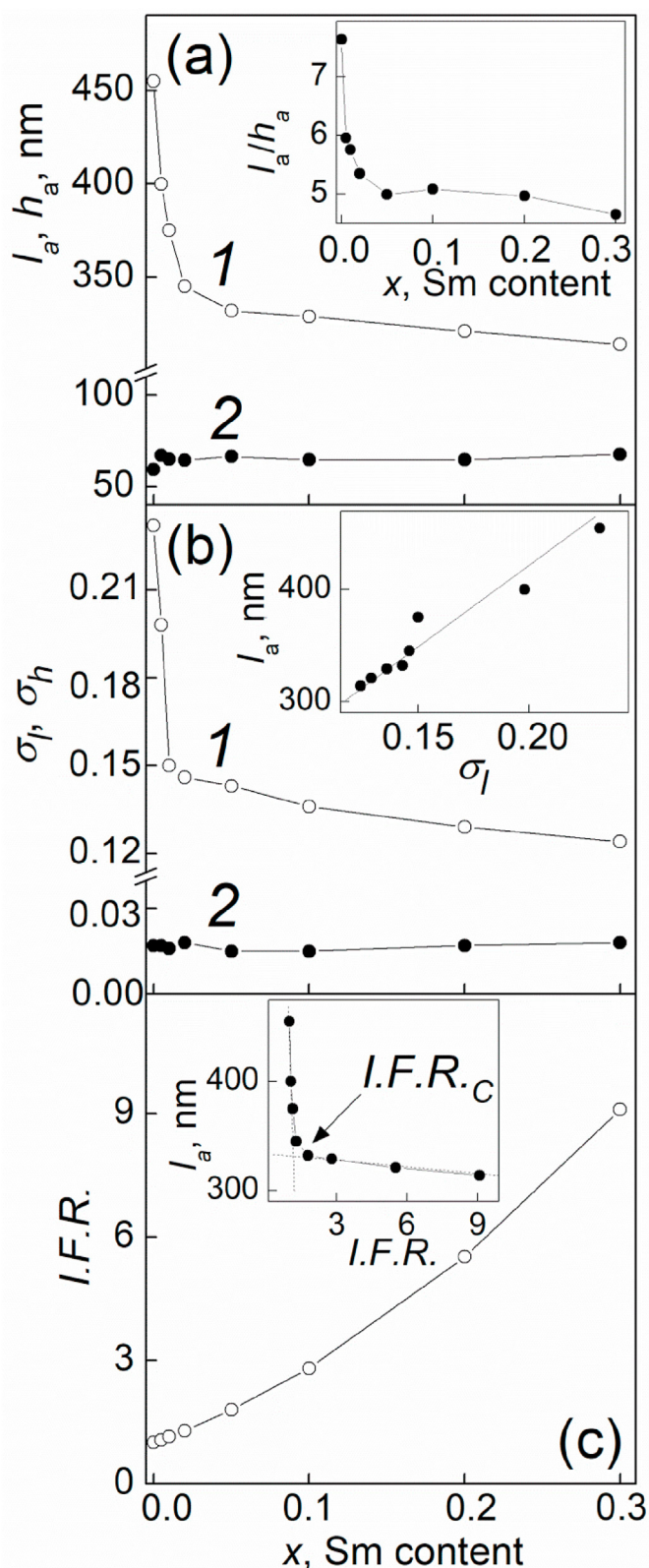
Fig. 2. (a) The Sm-doping effect on average lateral size, l_a, (curve *1*) and average thickness, h_a, (*2*) of the particles in the starting $Bi_{2-x}Sm_xTe_{2.7}Se_{0.3}$ powders. Inset shows the l_a/h_a vs. *x* dependence. (b) The Sm-doping effect on standard deviations for the *l* (σ_l, curve *1*) and *h* (σ_h, *2*) distributions. Inset shows the *l* vs. σ_l dependence. (c) The Sm-doping effect on change in ionic fraction in polar covalent Bi(Sm)-Te bond, *I.F.R.* Inset shows the l_a vs. *I.F.R.* dependence.

for the *l* (σ_l, curve *1*) and *h* (σ_h, *2*) distributions, which were extracted for different *x*, are presented in Fig. 2 (b). The σ_h is *x*-independent and small enough, i.e. the *F(h)* distribution is narrow. The σ_l is much more as compared to σ_h and it is *x*-dependent. Moreover, the $\sigma_l(x)$ dependence qualitatively corresponds to the $l_a(x)$ dependence. As result, increasing σ_l is accompanied by increasing l_a (inset to Fig. 2 (b)). The $l_a(\sigma_l)$ dependence is close to linear one, as is shown by solid line in inset. That is the Sm-doping results in gradually narrowing the *F(l)* distribution.

The Sm-doping effect on the particles size was already reported earlier in Ref. [28]. To analyse this effect, difference in the electronegativity of host Bi atoms and dopant Sm atoms was taken into account. Namely, this difference can affect strength of polar covalent Bi(Sm)-Te bonds in Bi_2Te_3-based compounds. The hexagonal Bi_2Te_3 structure is usually described in terms of layered structure. The five individual atomic layers are positioned perpendicularly to *c*-axis (hence, base (*a–b*)-planes are oriented along the layers) and stacked in the following order

$$Te(1)–Bi–Te(2)–Bi–Te(1), \qquad (2)$$

where Te(1) and Te(2) denote two different sites for Te in crystal structure.

In each stack, the Te(2) atoms are octahedrally coordinated by the Bi atoms. The Te(1) atoms are covalently bonded with three Bi atoms on one side the stack, and by weaker Van-der-Waals bonds with three other Te(1) atoms on the other side, which belongs to neighboring stack. The Bi–Te(1) bond length is close to the expected value for covalent bond length, while the Bi–Te(2) bond rather corresponds to the value that is expected for ionic bond [48,49].

Strictly speaking, both the Bi–Te(1) bond and the Bi–Te(2) bond are polar covalent bonds, which are different in a degree of ionic bonding. Solvothermal synthesis of Bi_2Te_3-based compounds is accompanied by forming and growth of nucleuses in a solution. Basic processes of this synthesis can be described in framework of "monoatom model" [50]. In accordance with the model, individual atoms or ions are combined to the Bi_2Te_3 nucleus, which grows in the solution, and then other atoms or ions attach to the nucleus, resulting in growth of the Bi_2Te_3 particle. When individual Te atom (or Te^{2-} ion) attaches itself to a Te(1)-layered crystal surface, this atom (or this ion) will probably jump back into the solution, since the Van-der-Waals bond is weak to fix the atom (or the ion) on surface, coinciding with base (*a–b*)-plane. However, interlayered Bi–Te(1) or Bi–Te(2) interaction in polar covalent bonds, existing within the stack, is strong enough to fix the atom or ion on lateral surface of the Bi_2Te_3 nucleus. Therefore, a lateral growth of the Bi_2Te_3 particles will be remarkably accelerating. As result, the Bi_2Te_3 particles (or the particles of Bi_2Te_3-based compounds) will grow faster in (*a–b*)-plane than in direction of *c*–axis, resulting in the hexagonal plate-shaped particles, as shown in inset to Fig. 1. Since the Bi–Te(1) and especially Bi–Te(2) bonds are polar covalent bonds, ionic bonding partially exists in the Bi_2Te_3 particles and these particles can possess the properties of ionic crystals. Ionic boding fraction (*I.F.*) in polar covalent bonding can be estimated by the empirical Pauling expression. In accordance with this expression, *I.F.* is related to a difference in the electronegativity of interacting *A* and *B* atoms (ions) as follows [51].

$$I.F. = 1 - \left[exp\left\{ -\frac{(\Delta X)^2}{4} \right\} \right] \times 100\% \qquad (3)$$

where X_A and X_B are the electronegativities of atoms (ions), and $\Delta X = X_A - X_B$.

The electronegativities of atoms in the $Bi_{2-x}Sm_xTe_{2.7}Se_{0.3}$ compounds are $X_{Bi} = 2.02$, $X_{Sm} = 1.17$, $X_{Te} = 2.10$ and $X_{Se} = 2.55$ [52]. Since $X_{Sm} > X_{Bi}$, *I.F.* will be gradually increasing with increasing *x*. Expression (3) can be applied to roughly estimate changing in *I.F.*, related to the Sm-doping.

To do so, difference in Te(1)-Bi and Te(2)-Bi bonds mentioned above will be neglected. The $X_{Bi-Sm} = [(1-x) \bullet X_{Bi} + x \bullet X_{Sm}]$ expression can be introduced to take into account changing in the X_{Bi} and X_{Sm} contributions to total electronegativity of the Sm-doped compounds with different x. The $X_{Te-Se} = [0.9 \bullet X_{Te} + 0.1 \bullet X_{Se}]$ expression can be also applied to take into account different electronegativities of Te and Se. As result, ΔX can be calculated as $\Delta X = X_{Bi-Sm} - X_{Te-Se}$. The calculated I.F. values are small, but relative changing in I.F. is remarkable. To show this changing in detail, I.F. was recalculated to I.F.R. $= I.F.(x)/I.F.(x = 0)$. The I.F.R. vs. Sm content dependence is presented in Fig. 2 (c). I.F.R is steady growing with increasing x. Inset to Fig. 2 (c) shows the l_a versus I.F.R. dependence. This dependence can be divided by two linear segments, as is shown by dashed lines in inset. Similarly to the $l_a(x)$ dependence, for I.F.R.<1.79 (this value corresponds to $x = 0.05$), l_a is very rapidly falling with increasing I.F.R, but for I.F.R.≥1.79, l_a is falling much more slowly. The I.F.R.$_C$ value, indicated by arrow in inset, corresponds to a crossover from the strong l_a(I.F.R.) dependence with $\Delta l_a / \Delta (I.F.R.) \approx 700$ nm to the weak l_a(I.F.R.) dependence $\Delta l_a / \Delta (I.F.R.) \approx 2.5$ nm.

In general, during a synthesis of ionic crystals from polar solutions, growth and dissolution processes are simultaneously competing [53–55]. In this case, the size and shape of the particles being growing is governed by result of this competition. Reducing in average lateral size of the particles in the starting $Bi_{2-x}Sm_xTe_3$ powders can be attributed to changing in dissolution process. The poly(1-ethenylpyrrolidin-2-one) solution, applied to solvothermally synthesize the $Bi_{2-x}Sm_xTe_3$ particles, is polar. The dissolution process is known to be based on an electrostatic interaction between ions, which are containing in the particles being growing, and polar molecules, which are containing in the solution [55]. Increasing in the ionic boding fraction can enhance the electrostatic interaction. As result, the dissolution process will become more effective. With increasing in I.F.R., average lateral size of the particles will be reducing that is, in turn, governed by increasing in Sm content. The growth and dissolution processes are x-dependent in complicated manner that results in relevant complicated behaviour of the $l_a(x)$ dependence or the l_a versus I.F.R. dependence, which consists of two parts. For part of the strong l_a versus I.F.R. dependence, the dissolution processes is dominant that results in rapidly reducing l_a. However, for part of the weak l_a versus I.F.R. dependence, l_a is changing much more slowly due to, probably, weakening of the dissolution processes (or enhancing of the growth process). Further experiments should be carried out to correctly analyse changing in l_a in the starting $Bi_{2-x}Sm_xTe_{2.7}Se_{0.3}$ powders with different x. Anyway, the Sm-doping limits the growth of the $Bi_{2-x}Sm_xTe_{2.7}Se_{0.3}$ particles for all x values. In this case, the histogram of the $F(l)$ distribution will be cut off for the big l values. As result, the width of the distribution will be decreasing that is in agreement with experimental data (Fig. 2 (b)).

The Ostwald ripening model is often applied to describe a growth of particles in various solutions [56,57]. In accordance with this model, a change in particle size with spherical shape can be expressed as

$$\langle R \rangle^3 = R_o^3 + \frac{8 \gamma C_\infty v^2 D}{9 R_g T} t \tag{4}$$

where $\langle R \rangle$ is the average radius of particles, γ is the surface energy per unit area (J·m^{-2}), c_∞ is the equilibrium solubility, ν is the molar volume of the particle's material, D is the diffusion coefficient, R_g is the ideal gas constant, T is the temperature, and t is the growth time.

One can see that decreasing in c_∞ should result in relevant reducing in particle size. Since with increasing x in the $Bi_{2-x}Sm_xTe_3$ compounds, c_∞ can be decreasing through increasing in the ionic boding fraction, size of the $Bi_{2-x}Sm_xTe_3$ particles will be reducing, too. To analyse a growth of Ce-doped SnO_2 nanocrystals synthesized by Pechini's method, expression (4) was earlier modified as follows [57].

$$\langle R \rangle^3 = R_o^3 + k \cdot exp(-Ax) \tag{5}$$

where $\langle R_0 \rangle$, k and A are the fitting parameters and x is the Ce content.

The surface energy was assumed to be a dominant parameter for the particle size reduction in Ce-doped SnO_2 nanocrystals. The dopant enrichment of the nanocrystal surface was considered as key mechanism affecting the surface energy. We also applied expression (5) to describe the Sm doping effect on average volume, V_p, of the $Bi_{2-x}Sm_xTe_3$ particles. To calculate V_p, the particles are believed to be cylinder-shaped. Then, V_p can be calculated as $V_p(x) = (\pi l_a^2 / 4) h_a$. The V_p versus x dependence is shown in Fig. 3. With $V_p = 6.86 \cdot 10^6$ nm^3, $k = 5.55$ nm^3 and $A = 85$, expression (5) well describes experimental curve.

In general, strong exponential x-dependence of V_p can be attributed to forming of critical nucleuses in solution. The critical nucleus has a critical radius corresponding to minimum particle size from which an aggregate of atoms or ions is thermodynamically stable. During a chemical synthesis, these critical nucleuses will be clustering together resulting in growth of particles. Therefore, under gradual Sm doping, size of the $Bi_{2-x}Sm_xTe_{2.7}Se_{0.3}$ particles will be reducing but with saturating to constant value, limited by size of critical nucleuses.

3.2. Links between particles in starting powders and grain structure in the textured $Bi_{2-x}Sm_xTe_{2.7}Se_{0.3}$ samples

Density of all the bulk $Bi_{2-x}Sm_xTe_{2.7}Se_{0.3}$ samples, SPS-prepared from the starting powders with different l_a, happened to be weakly and irregularly x-dependent. Maximum value of density is equal to ~7.75 g·cm^{-3} for $x = 0.3$ that is ~99.4% of theoretical value of the Bi_2Te_3 density (7.78 g/cm^3, according to Ref. [22]). 7.7 g/cm^3), and minimum value is ~6.78 g·cm^{-3} for $x = 0.02$ (~87%). Similarly to XRD patterns of the starting powders, XRD patterns for all the bulk samples correspond to the space symmetry $R\bar{3}m$ group, too. However, the lattice $a = b$ and c parameters are x-dependent (Fig. S1). With increasing x, the c parameter increases, whereas the a parameter is x-independent. This behaviour can be associated with difference in radii of Sm and Bi. The radii of Sm (ionic Sm^{3+} radius is 1.08 Å and covalent radius is 1.62 Å) are bigger than the radii of Bi (ionic Bi^{3+} radius is 1.03 Å and covalent radius is 1.46 Å) [58]. As result, under gradual substitution of Sm for Bi, a volume of unit cell should be slightly increasing.

All the SPS-sintered samples were found to be highly textured. Usually, the texturing is developing under uniaxial mechanical loading starting powders of Bi_2Te_3-based compounds, consisting of 2D-particles [59]. Under SPS process, the uniaxial loading and sintering process are
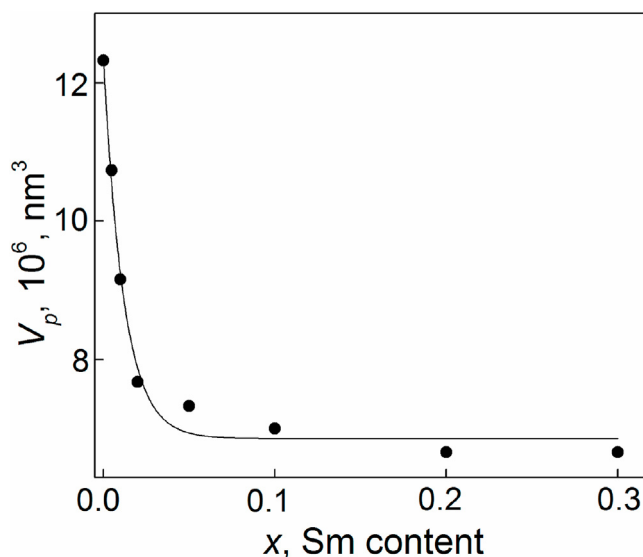

Fig. 3. The Sm-doping effect on average volume of the particles in the starting $Bi_{2-x}Sm_xTe_{2.7}Se_{0.3}$ powders. Solid line is fitting curve.

acting simultaneously. A texturing axis coincides with mechanical loading direction. The texturing results in preferential ordering of the plate-like grains, forming specific lamellar sheets, which lie in a plane perpendicular to the texturing axis. Crystal c-axes of the grains are preferentially directed parallel to the texturing axis, while crystal (a-b)-planes of the same grains are preferentially oriented perpendicularly to this direction. The texture can be clearly observed via SEM examination of surfaces, oriented perpendicularly and parallel to the texturing axis. As an example, these SEM images, taken for perpendicular (top images) and parallel (bottom images) surfaces of the $Bi_{2-x}Sm_x$-$Te_{2.7}Se_{0.3}$ samples with $x = 0$, 0.1 and 0.3 are shown in Fig. 4. The images are characteristic for textured Bi_2Te_3-based compounds. Namely, a disordered grain structure with irregularly shaped grains is observed for the perpendicular surface, whereas the plate-like grains, forming the lamellar sheets, are observed for the parallel surface. Owing to the texturing, average grain sizes, measured in directions parallel ($D_\perp$) and perpendicular (D∥) to the texturing axis, are quite different. Moreover, these sizes happened to be x-dependent. To correctly estimate $D_\perp$ and D∥, EBSD-SEM (electron back scattered diffraction-scanning electron microscopy) maps were taken from thoroughly polished surfaces of the textured $Bi_{2-x}Sm_xTe_{2.7}Se_{0.3}$ compounds with different x. These maps show distribution of crystallographic orientations of the surface grains. As an example, EBSD-SEM maps, taken from the surfaces oriented parallel to the texturing axis for textured $Bi_2Te_{2.7}Se_{0.3}$ and $Bi_{1.98}Sm_{0.02}$-$Te_{2.7}Se_{0.3}$ samples, are presented in Fig. 5. A colour of individual grain is directly connected with its crystallographic orientations in accordance with inset to Fig. 5.

One can see that increasing Sm content results in remarkably decreasing the grain size. By using EBSD-SEM maps, histograms of the grain size distributions, corresponding to perpendicular and parallel surfaces, were plotted for the samples with different x (Fig. S2). The lognormal unimodal distribution based on expression (1) was again applied to analyse the histograms and extract $D_\perp$ and D∥, as well as standard deviations, $\sigma_{D\perp}$, and $\sigma_{D\text{II}}$, for these distributions. The $D_\perp(x)$ and D∥(x) dependences are presented in Fig. 6 (a). Both sizes are steady reducing with increasing x. These dependences behave similarly to the $l_a(x)$ dependence, extracted for particles in the starting powders (Fig. 2 (a)). For small x values ($x < 0.02$), $D_\perp$ and D∥ are very rapidly falling with increasing x, but for $x \geq 0.02$, they start falling much more slowly. $D_\perp$ changes from ~2230 nm for $x = 0$–~970 nm for $x = 0.3$. These $D_\perp$ values

correspond to micrograined structures. D∥ changes from ~440 nm for $x = 0$–~75 nm for $x = 0.3$, i.e. with increasing x, gradual crossover from micrograined to nanograined structures takes place. To characterize shape of the grains in the textured $Bi_{2-x}Sm_xTe_{2.7}Se_{0.3}$ samples, grain shape factor, $D_\perp/D∥$, was introduced. The $D_\perp/D∥$ versus x dependence is shown in inset to Fig. 6 (a). With increasing x, $D_\perp/D∥$ is non-monotonically increasing. This x-dependent behaviour is opposite to that for the particle shape factor, l_a/h_a, in the starting powders (inset to Fig. 2 (a)). For all the compositions, $D_\perp/D∥ \gg 1$, i.e. the grains in the textured $Bi_{2-x}Sm_xTe_{2.7}Se_{0.3}$ samples are 2D-objects. The standard $\sigma_{D\perp}$ and $\sigma_{D\text{II}}$ deviations are presented in Fig. 6 (b). With increasing x, $\sigma_{D\perp}$ and $\sigma_{D\text{II}}$ are changing in the same manner, as $D_\perp$ and D∥. As result, increasing in $\sigma_{D\perp}$ and $\sigma_{D\text{II}}$ are accompanied by increasing in $D_\perp$ and D∥, respectively. The $D_\perp(\sigma_{D\perp})$ dependence is presented in inset to Fig. 6 (b).

There are links between the particles the starting $Bi_{2-x}Sm_xTe_{2.7}Se_{0.3}$ powders and the grain structure in the relevant textured samples. These links include, firstly, "particle size"→"grain size" link and, secondly, "particle size"→"preferential grain orientation" link. According to the first link, the bigger particles in the starting powders naturally correspond to the bigger grains in relevant bulk samples (Fig. 7 (a)). Since the thickness of the particles is x-independent, this link is well expressed for the $D_\perp$ and l_a values (curve 1 in Fig. 7 (a)). The link between the D_{II} and h_a values is close to vertical line (curve 2). Generally, forming of the grain structure is due to grain growth process during a high-temperature sintering a starting powder. The grain growth is accompanied by reducing in energy of system having numerous interfaces. This energy is expressed as γA, where γ is specific energy of the interface and A is surface area of the interface.

During the grain growth, particles of the starting powder preserve their original form, but they change in size by coalescence, that results in reducing the surface areas. The high-temperature grain growth can be described by expression [60].

$$D_t^n - D_0^n = Ct\exp\left(-\frac{E_a}{RT}\right) \tag{6}$$

where D_t and D_0 are the average grain size at time t and the original grain size, respectively, n is the grain growth exponent, t is the sintering time, E_a is the activation energy of the grain growth, C is the pre-exponential constant and R is the general gas constant.
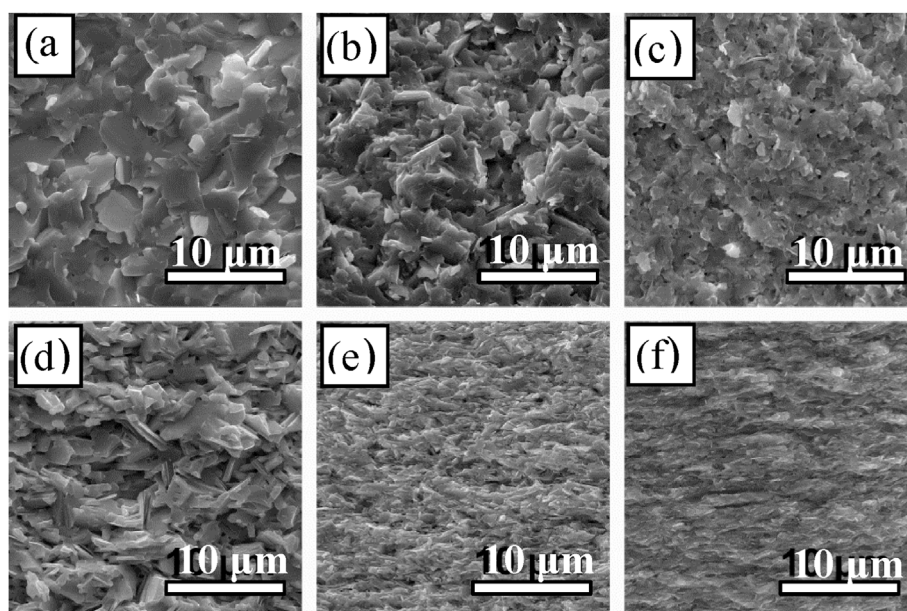

Fig. 4. SEM images taken on the fractured surfaces of the $Bi_{2-x}Sm_xTe_{2.7}Se_{0.3}$ samples with $x = 0$ ((a) and (d)), 0.1 ((b) and (e)) and 0.3 ((c) and (f)), which are oriented parallel (top images) and perpendicularly (bottom images) to the texturing axis.
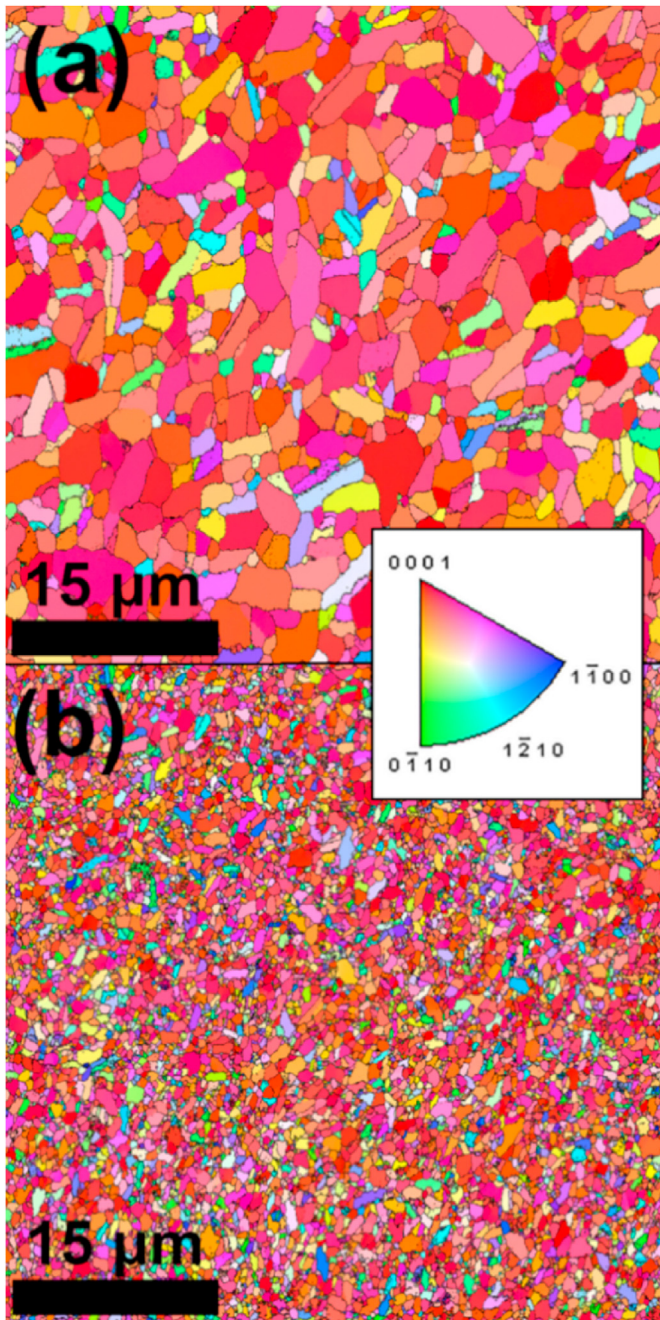
Fig. 5. EBSD-SEM maps, taken from the surfaces oriented parallel to the texturing axis for the bulk $Bi_2Te_{2.7}Se_{0.3}$ (a) and $Bi_{1.98}Sm_{0.02}Te_{2.7}Se_{0.3}$ (b) samples. Inset shows a link between color of the drain and its crystallographic orientation.

According to inset to Fig. 6 (a), with increasing x, $D_\perp/D_\parallel$ is non-monotonically increasing, i.e. shape of the grains becomes more aniso-tropic. This $D_\perp/D_\parallel$ versus x behaviour can be originated from different values on average rates of the grain growth in directions perpendicular ($RG_\perp$) and parallel ($RG_\parallel$) to the texturing axis. These rates can be expressed as

$$RG_\perp = \frac{D_\perp - l_a}{t_s} \text{ and } RG_\parallel = \frac{D_\parallel - h_a}{t_s} \tag{7}$$
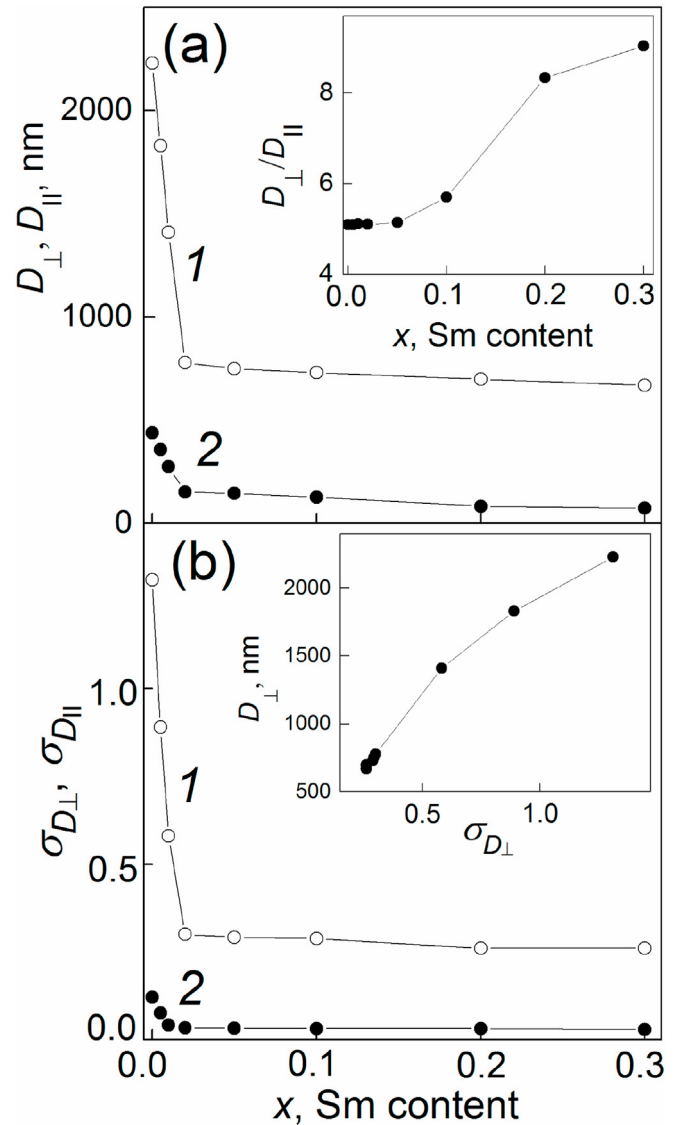
where $t_s = 150$ s is holding time at SPS process.

Fig. 6. (a) The Sm-doping effect on average grain sizes in the textured $Bi_{2-x}Sm_xTe_{2.7}Se_{0.3}$ samples, measured in directions perpendicular ($D_\perp$, curve *1*) and parallel ($D_\parallel$, curve *2*) to the texturing axis. Inset shows the $D_\perp/D_\parallel$ vs. x dependence. (b) The Sm-doping effect on standard deviations for the $D_\perp$ ($\sigma_{D\perp}$, curve *1*) and $D_\parallel$ ($\sigma_{D\parallel}$, *2*) distributions. Inset shows the $D_\perp$ vs. $\sigma_{D\perp}$ dependence.

The Sm-doping effect on $RG_\perp$ and $RG_\parallel$ is illustrated by Fig. 7 (b). Since $RG_\perp > RG_\parallel$, perpendicular grain growth is faster than parallel one. To explain this feature, mechanism of the grain growth should be correctly identified. At present, it is rather complicated task.

To examine the Sm-doping effect on the preferential grain orientation (the texturing degree) in the bulk $Bi_{2-x}Sm_xTe_{2.7}Se_{0.3}$ samples, the Lot-gering factor, LF, was calculated via analysis of XRD patterns, taken from the surface perpendicular to the texturing axis for the compositions with different x [61] (Fig. S3). The $LF(x)$ dependence is presented in Fig. 8 (a). With increasing Sm content, LF is gradually increasing. This Sm-doping effect on the texturing degree of $Bi_2Te_{2.7}Se_{0.3}$ was earlier reported in Ref. [28]. It was attributed to reducing in the lateral size of the particles in the starting $Bi_{2-x}Sm_xTe_{2.7}Se_{0.3}$ powders under gradual Sm-doping. The $LF(l_a)$ dependence, obtained in present work, is shown in Fig. 8 (b). With increasing l_a, LF is rapidly decreasing. Mechanism, which results in this $LF(l_a)$ dependence is briefly illustrated in Fig. S4.
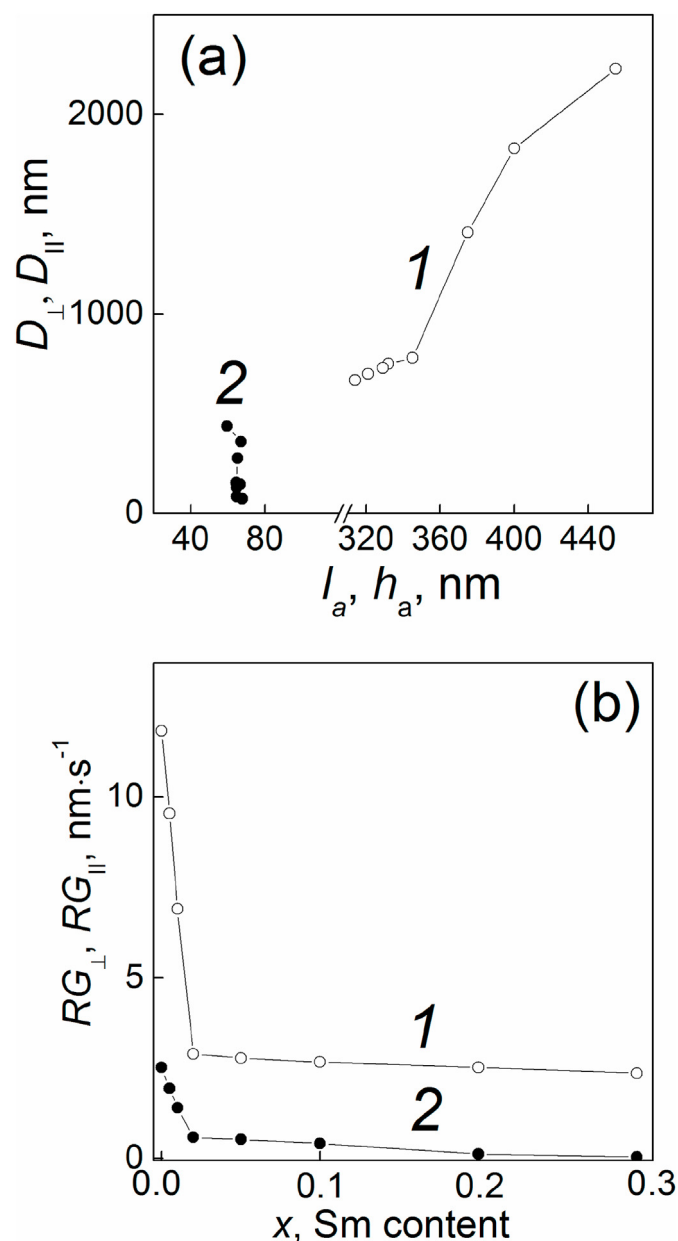
Fig. 7. (a) The $D_\perp$ vs. l_a (curve *1*) and D_{II} vs. h_a (*2*) dependences for the textured $Bi_{2-x}Sm_xTe_{2.7}Se_{0.3}$ samples; (b) The Sm-doping effect on average rates of the grain growth in directions perpendicular ($RG_\perp$, curve *1*) and parallel (RG_{II}, curve *2*) to the texturing axis.

3.3. Grain size effect on transport properties of the textured $Bi_{2-x}Sm_xTe_{2.7}Se_{0.3}$ samples

Thus, the Sm-doping allows preparing the textured $Bi_{2-x}Sm_xTe_{2.7}Se_{0.3}$ samples with different grain size. These samples can be applied to examine various grain size effects on their physical properties. If some grain effect really occurs, the relevant physical property will be crucially sensitive to the grain size via involving various physical mechanisms. Usually, these grain size effects are remarkably observed in fine-grained solids. Moreover, reducing the grain size will result in enhancing the grain size effect. For instance, the specific electrical resistivity in grained materials often demonstrates the grain size effect on ρ (Fig. S5). This effect, which is due to electron scattering by grain boundaries, will be implementing, when electron free mean path will be approaching to the grain size. The grain size effect was also found in the transport properties of the textured $Bi_{2-x}Sm_xTe_{2.7}Se_{0.3}$ samples with different grain size.

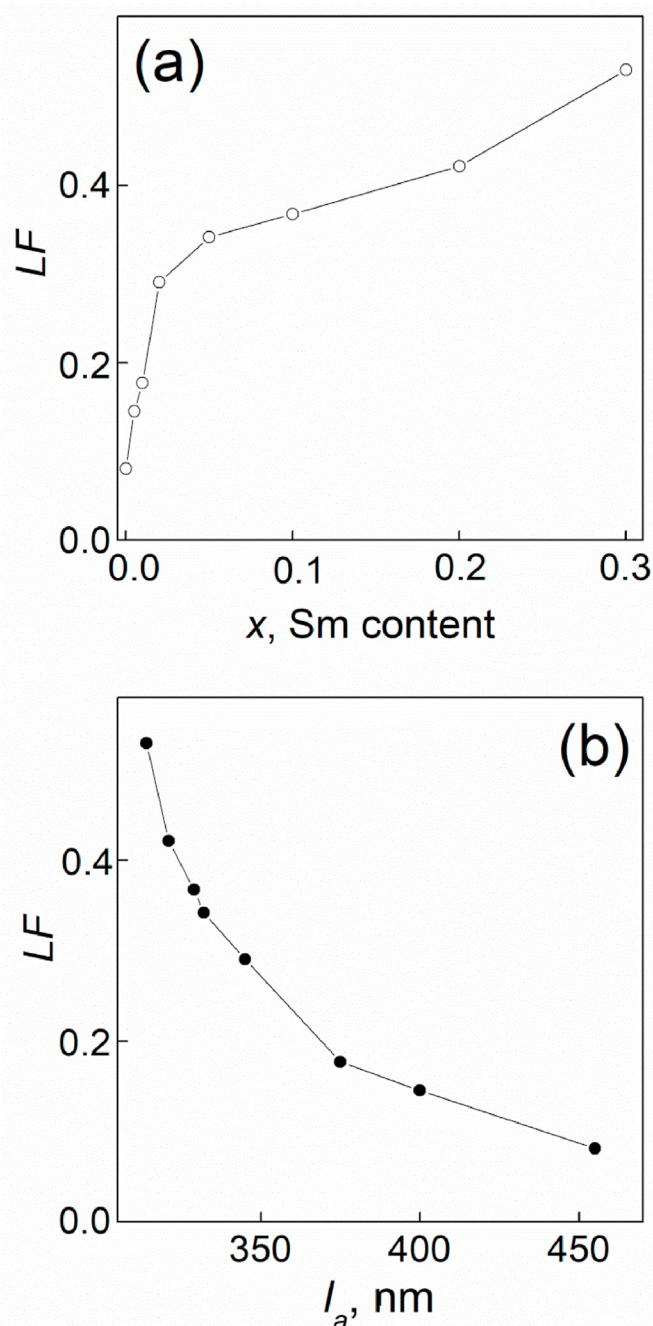**Fig. 8.** (a) The Sm-doping effect on the Lotgering factor for the textured $Bi_{2-x}Sm_xTe_{2.7}Se_{0.3}$ samples. (b) The *LF* vs. l_a dependence.

Owing to the layered structure, single-crystalline Bi_2Te_3 and Bi_2Te_3-based compounds are high-anisotropic [36]. Anisotropy in the transport properties can be characterized by anisotropy coefficients, *AC*. For the specific electrical resistivity and the total thermal conductivity these coefficients can be introduced as the ρ_c/ρ_{ab} and k_{ab}/k_c coefficients (the *c* and *ab* subscripts correspond to the directions perpendicular or parallel to the layers, respectively) [60].

For grained material with completely random orientation of the grains, the transport properties are isotropic. Preferential grain orientating in textured Bi_2Te_3 and Bi_2Te_3-based compounds can partially recover the anisotropy in the transport properties. As result, these properties, measured perpendicularly (perpendicular measuring orientation, $\rho_\perp$ and $k_\perp$) or parallel to the texturing axis (parallel measuring orientation, ρ_{II} and k_{II}), are different. As was mentioned above, the
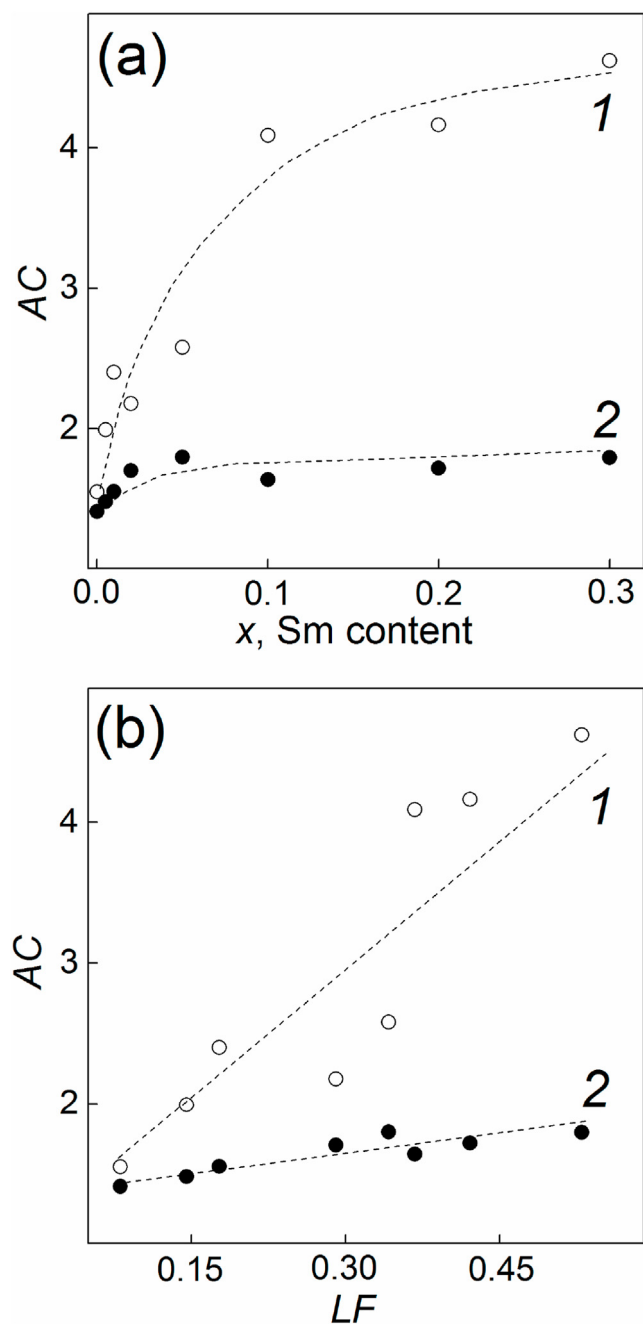
Fig. 9. (a) The Sm-doping effect on the anisotropy coefficients for the specific electrical resistivity (curve *1*) and the total thermal conductivity (*2*); (b) Dependences of these coefficients on the Lotgering factor.

Fig. 10. The grain size effects on the transport properties of the textured Bi$_{2-x}$Sm$_x$Te$_{2.7}$Se$_{0.3}$ samples: (a) the $\rho_\perp$ vs. $D_\perp$ (curve *1*) and ρ_{II} vs. D_{II} dependences; (b) The $k_\perp$ vs. $D_\perp$ (*1*) and k_{II} vs. D_{II} dependences (*2*); (c) The $k_{e\perp}$ vs. $D_\perp$ (*1*), k_{eII} vs. D_{II} (*2*), $k_{p\perp}$ vs. $D_\perp$ (*1'*), k_{pII} vs. D_{II} (*2'*) dependences.

texturing axis for SPS-prepared compounds coincides with the pressing direction during SPS-process. The Sm-doping effect on the *AC* for the specific electrical resistivity (curve *1*) and the total thermal conductivity (*2*) is shown in Fig. 9 (a). Anisotropy in the transport properties is increases with increasing *x*. This behaviour is mainly originated from increasing in the Lotgering factor under gradual Sm-doping, i.e. higher degree of grain orienting in the textured samples is expectedly accompanied by higher anisotropy in the transport properties.

The $\rho_\perp$ versus $D_\perp$ and ρ_{II} versus D_{II} dependences, as well as the $k_\perp$ versus $D_\perp$ and k_{II} versus D_{II} dependences, taken at room temperature for the textured Bi$_{2-x}$Sm$_x$Te$_{2.7}$Se$_{0.3}$ samples, are presented in Fig. 10 (a) and (b). The grain size effect on the transport properties is clearly observed in

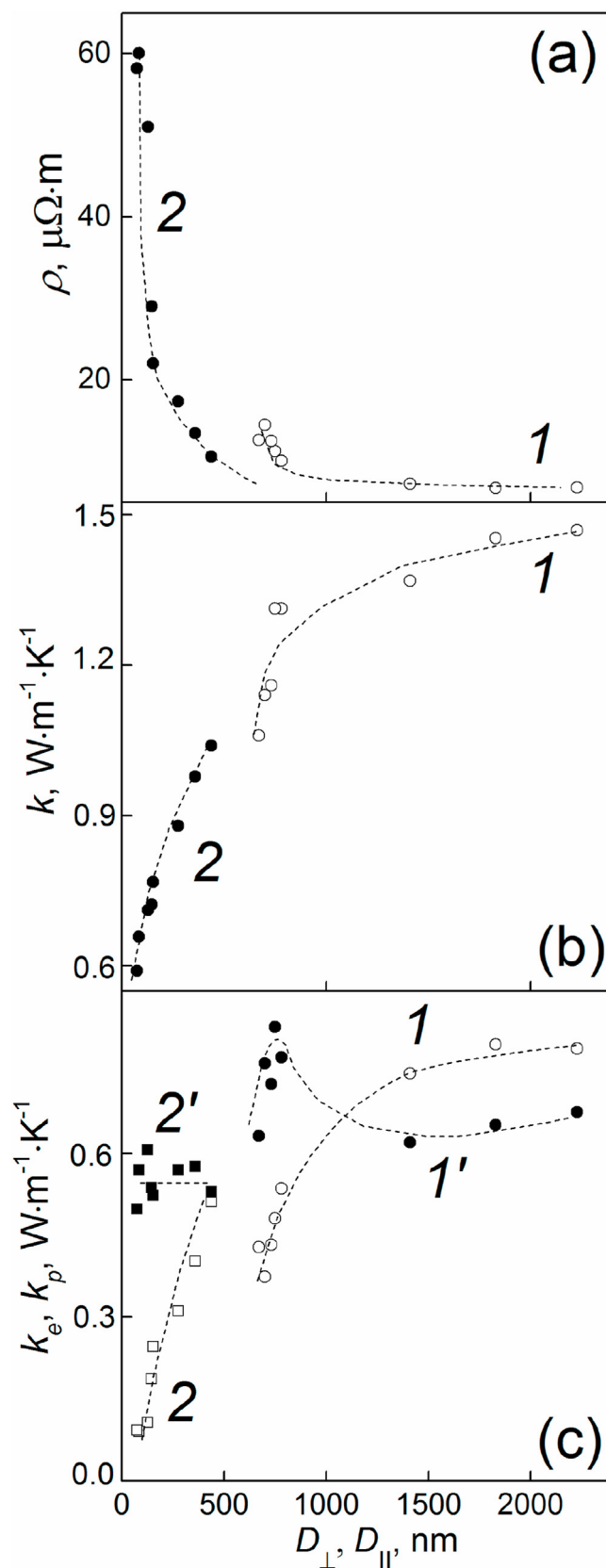these dependences. This effect is much more expressed for the parallel measuring orientation, corresponding to the samples with fine-grained structures. For this orientation, ρ_{II} is rapidly increasing, and k_{II} is rapidly decreasing with decreasing D_{II}. For the perpendicular measuring orientation, corresponding to the samples with coarse-grained structures, $\rho_\perp$ and $k_\perp$ are changing much more slowly with changing $D_\perp$. Moreover, with increasing the grain sizes, $\rho_\perp$ and $k_\perp$ becomes very weakly $D_\perp$- and D_{II}-dependent. At room temperature, the total thermal conductivity is combined by contributions from the electronic thermal conductivity, k_e, and the phonon thermal conductivity, k_p, i.e. $k = k_e + k_p$. The k_e contribution is related to the specific electrical resistivity through the Wiedemann-Franz law

$$k_e = \frac{LT}{\rho} \tag{8}$$

where L is the Lorenz number.

For the $Bi_{2-x}Sm_xTe_{2.7}Se_{0.3}$ compounds, L was earlier estimated as $\sim 1.8 \times 10^{-8}$ WΩ·K^{-2} for all the x values. Using this L value and expression (8), the k_e and k_p contributions into $k_\perp$ and k_{II} were extracted. The $k_{e\perp}$ versus $D_\perp$ and $k_{e\mathrm{II}}$ versus D_{II}, $k_{p\perp}$ versus $D_\perp$ and $k_{p\mathrm{II}}$ versus D_{II} dependences are presented in Fig. 10 (c). The behaviour of the electronic contributions is in agreement with behaviour of the total thermal conductivity, i.e. the similar grain size effect on the electronic thermal conductivity is also observed. However, no grain size effect on the

phonon thermal conductivity can be found. The k_p contribution is due to a heat transfer by phonons. Therefore, the grain boundaries in the textured $Bi_{2-x}Sm_xTe_{2.7}Se_{0.3}$ samples are much less effective centres to scatter phonons compared to electrons. This difference can be attributed to different values of electron free mean path and phonon free mean path.

Increasing in Sm content in the $Bi_{2-x}Sm_xTe_{2.7}Se_{0.3}$ compounds can be also accompanied by change in electron concentration, n. The Sm-doping effect on n can also affect the specific electrical resistivity and the electronic thermal conductivity. To estimate this effect, the Hall effect was examined. The $n(x)$ dependence is presented in Fig. 11 (a).

The electron concentration is steady falling with increasing x. Owing to high-temperature Te evaporation, the Bi_2Te_3-based compounds usually are nonstoichiometric Te-deficient ones. For the nonstoichiometric Te-deficient $Bi_{2-x}Sm_xTe_{2.7}Se_{0.3}$ compounds, the vacancies at Te sites, $V_{Te}^{\cdot\cdot}$, are the most common defects [62]. Forming each positively charged $V_{Te}^{\cdot\cdot}$ vacancy leaves two free electrons, resulting in n-conductivity. With increasing x, a rate of the Te evaporation will be decreasing that is related to difference in electronegativites of the Bi and Sm atoms, which, in turn, results in increasing the strength of polar covalent Sm–Te bond as compared to that for polar covalent Bi–Te bond. This effect was recently observed in the $Bi_{2-x}Gd_xTe_{3-y}$ compounds [63]. Decreasing in the rate of the Te evaporation results in relevant decreasing in number of the $V_{Te}^{\cdot\cdot}$ vacancies. Therefore, the electron concentration will be also decreasing. This behaviour was observed in our experiment (Fig. 11 (ao)). The $n(x)$ dependence was applied to find the Sm-doping effect on the Hall mobility of electrons. Due to anisotropy in ρ for the textured samples, two values of the Hall mobility corresponding to the perpendicular ($\mu_{H\perp}$) and parallel ($\mu_{H\mathrm{II}}$) orientations were calculated. The $\mu_{H\perp}(T_S)$ and $\mu_{H\mathrm{II}}(T_S)$ dependences are also presented in Fig. 11 (a). With increasing x, both Hall mobilities are decreasing with gradual saturating to constant values. The $\mu_{H\mathrm{II}}(D\mathrm{II})$ and $\mu_{H\perp}(D_\perp)$ dependences are shown in Fig. 11 (b). Grain size effect on the electron mobilities is clearly observed in these dependences. Therefore, grain size effect on the specific electrical resistivity and the electronic thermal conductivity can be mainly attributed to relevant grain size effect on the electron mobilities.

4. Conclusion

Solvothermal synthesis and spark plasma sintering of starting powders were applied to prepare the textured $Bi_{2-x}Sm_xTe_{2.7}Se_{0.3}$ compounds with $x = 0$; 0.005; 0.01; 0.02; 0.05; 0.1; 0.2 and 0.3. The Sm-doping results in developing several interconnected effects as follows:

(a) With increasing x, reducing in the particles size in the starting powders takes place. This effect can be originated from increasing in ionic bonding fraction in polar covalent Bi(Sm)-Te bonds, which occurs at increasing Sm content due to a difference in electronegativity of atoms Bi and Sm. As result, under solvothermal synthesis in polar solution, dissolution process, which competes with growth process, becomes more effective, limiting growth of the $Bi_{2-x}Sm_xTe_{2.7}Se_{0.3}$ particles for all x values. With increasing x, reducing in the size grains in the bulk samples, which is governed by relevant changing in the particles size in the starting powders, takes place, too. This effect also results in enhancing in texturing degree in the samples at gradual increasing Sm content.

(b) Grain size effects on the specific electrical resistivity and the total thermal conductivity were found in the bulk samples with different grain sizes. These effects were measured parallel or perpendicularly to the texturing axis (direction of mechanical loading at spark plasma sintering). With increasing the grain size, the resistivity abruptly increases, whereas the total thermal conductivity and the electron thermal conductivity abruptly decrease. These features are connected with ability of grain boundaries act as scattering centres for electrons.
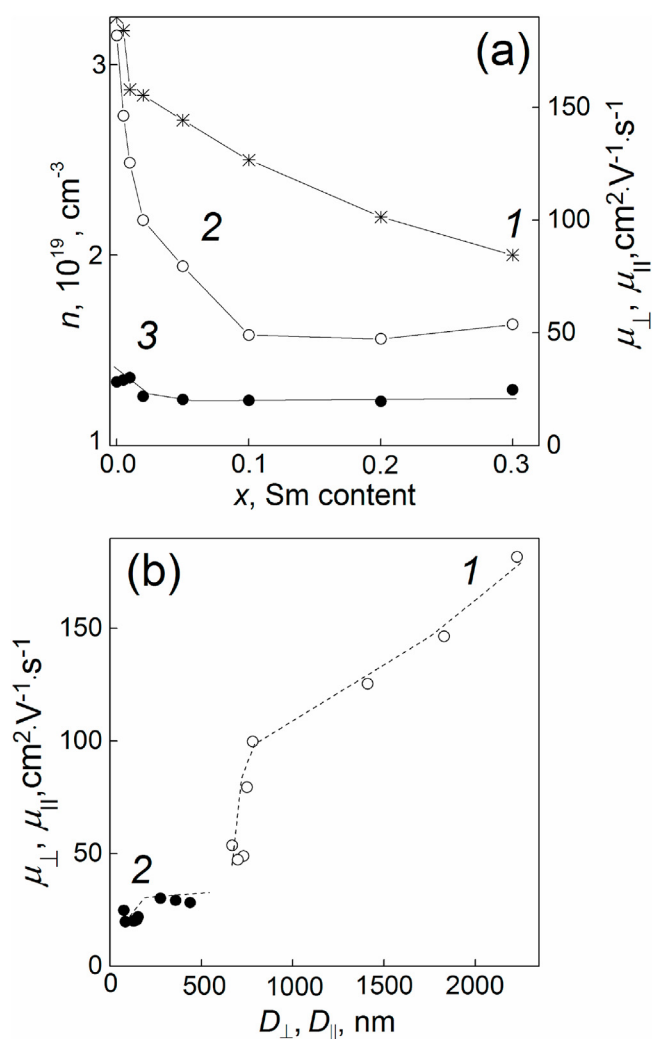
Fig. 11. (a) The Sm-doping effect on the electron concentration (curve *1*) and the Hall electron mobilities, measured perpendicularly (*2*) and parallel (*3*) to the texturing axis; (b) The $\mu_{H\perp}$ vs. $D_\perp$ (curve *1*) and $\mu_{H\mathrm{II}}$ vs. DII (*2*) dependences.

CRediT authorship contribution statement

Maxim Yaprintsev: Project administration, Investigation. **Alexei Vasil'ev:** Investigation. **Oleg Ivanov:** Conceptualization, Writing – review & editing. **Daniil Popkov:** Investigation.

Declaration of competing interest

The authors declare that they have no known competing financial interests or personal relationships that could have appeared to influence the work reported in this paper.

Acknowledgments

Appendix A. Supplementary data

Supplementary data to this article can be found online at https://doi.org/10.1016/j.jssc.2022.123176.

References

[1] G.J. Snyder, Figure of merit *ZT* of a thermoelectric device defined from materials properties, Energy Environ. Sci. 10 (2017) 2280–2283, https://doi.org/10.1039/c7ee02007d.

[2] W. Saito, K. Hayashi, J. Dong, J.F. Lee, Y. Miyazaki, Control of the thermoelectric properties of Mg_2Sn single crystals via point-defect engineering, 2020, Sci. Rep. 10 (2020) 1–8, https://doi.org/10.1038/s41598-020-58998-1.

[3] G. Guelou, C. Couder, A. Bourhim, O. Lebedev, N. Daneu, A scalable synthesis route for multiscale defect engineering in the sustainable thermoelectric quaternary sulfide Cu26V2Sn6S32, Acta Mater. 195 (2020) 229–239, https://doi.org/10.1016/j.actamat.2020.05.039.

[4] Y. Anno, Y. Imakita, K. Takei, S. Akita, T. Arie, Enhancement of graphene thermoelectric performance through defect engineering, 2D Mater. 4 (2017), 025019, https://doi.org/10.1088/2053-1583/aa57fc, 1-6.

[5] X. Dong, W. Cui, W.-D. Liu, S. Zheng, L. Gao, L. Yue, Y. Wue, B. Wang, Z. Zhang, L. Chen, Z.-G. Chen, Synergistic band convergence and defect engineering boost thermoelectric performance of SnTe, J. Mater. Sci. Technol. 86 (2021) 204–209, https://doi.org/10.1016/j.jmst.2021.01.040.

[6] Y. Pan, T.R. Wei, C.F. Wu, J.F. Li, Electrical and thermal transport properties of spark plasma sintered *n*-type $Bi_2Te_{3-x}Se_x$ alloys: the combined effect of point defect and Se content, J. Mater. Chem. C. 3 (2015) 10583–10589, https://doi.org/10.1039/C5TC02219C.

[7] L. Hu, T. Zhu, X. Liu, X. Zhao, Point defect engineering of high-performance bismuth-telluride-based thermoelectric materials, Adv. Funct. Mater. 24 (2014) 5211–5218, https://doi.org/10.1002/adfm.201400474.

[8] J. Suh, K.M. Yu, D. Fu, X. Liu, F. Yang, J. Fan, D.J. Smith, Y.H. Zhang, J.K. Furdyna, C. Dames, W. Walukiewicz, J. Wu, Simultaneous enhancement of electrical conductivity and thermopower of Bi_2Te_3 by multifunctionality of native defects, Adv. Mater. 27 (2015) 3681–3686, https://doi.org/10.1002/adma.201501350.

[9] Q. Song, J. Zhou, L. Meroueh, D. Broido, Z. Ren, G. Chen, The effect of shallow vs. deep level doping on the performance of thermoelectric materials, Appl. Phys. Lett. 109 (2016) 1–5, https://doi.org/10.1063/1.4973292, 263902.

[10] J.A. Grovogui, T.J. Slade, S. Hao, C. Wolverton, M.G. Kanatzidis, V.P. Dravid, Implications of doping on microstructure, processing, and thermoelectric performance: the case of PbSe, J. Mater. Res. 36 (2021) 1272–1284, https://doi.org/10.1557/s43578-021-00130-8.

[11] Y. Iwasaki, K. Kitahara, K. Kimura, Effects of Cu doping on thermoelectric properties of Al–Si–Ru semiconducting quasicrystalline approximant, 125401, Phys. Rev. Materials 5 (2021) 1–5, https://doi.org/10.1103/PhysRevMaterials.5.125401.

[12] J. Li, M.P. Garman, J. Dong, B. van der Zee, L. Qiu, G. Portale, J.C. Hummelen, L.J.A. Koster, Doping engineering enables highly conductive and thermally stable *n*-type organic thermoelectrics with high power factor, ACS Appl. Energy Mater. 2 (2019) 6664–6671, https://doi.org/10.1021/acsaem.9b01179.

[13] Y. Qin, L. Yang, J. Wei, S. Yang, M. Zhang, X. Wang, F. Yang, Doping fffect on Cu_2Se thermoelectric performance: a review, 5704, Materials 13 (2020) 1–32, https://doi.org/10.3390/ma13245704.

[14] J. Liu, T. Xing, Z. Gao, J. Liang, L. Peng, J. Xiao, P. Qiu, X. Shi, L. Chen, Enhanced thermoelectric performance in ductile Ag_2S-based materials via doping iodine, 121905, Appl. Phys. Lett. 119 (2021) 1–5, https://doi.org/10.1063/5.0065063.

[15] N. Neophytou, M. Thesberg, Modulation doping and energy filtering as effective ways to improve the thermoelectric power factor, J. Comput. Electron. 15 (2016) 16–26, https://doi.org/10.1007/s10825-016-0792-7.

[16] M. Yapryntsev, A. Vasil'ev, O. Ivanov, Sintering temperature effect on thermoelectric properties and microstructure of the grained $Bi_{1.9}Gd_{0.1}Te_3$ compound, J. Eur. Ceram. Soc. 39 (2019) 1193–1205, https://doi.org/10.1016/j.jeurceramsoc.2018.12.041.

[17] J. Yang, F. Wu, Z. Zhu, L. Yao, H. Song, X. Hu, Thermoelectrical properties of lutetium-doped Bi_2Te_3 bulk samples prepared from flower-like nanopowders, J. Alloys Compd. 619 (2015) 401–405, https://doi.org/10.1016/j.jallcom.2014.09.024.

[18] X.H. Ji, X.B. Zhao, Y.H. Zhang, B.H. Lu, H. Ni, Synthesis and properties of rare earth containing Bi_2Te_3 based thermoelectric alloys, J. Alloys Compd. 387 (2005) 282–286, https://doi.org/10.1016/j.jallcom.2004.06.047.

[19] F. Wu, H. Song, J. Jia, X. Hu, Effects of Ce, Y, and Sm doping on the thermoelectric properties of Bi_2Te_3 alloy, Prog. Nat. Sci. Mater. Int. 23 (2013) 408–412, https://doi.org/10.1016/j.pnsc.2013.06.007.

[20] F. Wu, W. Shi, X. Hu, Preparation and thermoelectric properties of flower-like nanoparticles of Ce-Doped Bi_2Te_3, Electron, Mater. Lett. 11 (2015) 127–132, https://doi.org/10.1007/s13391-014-4139-x.

[21] X.H. Ji, X.B. Zhao, Y.H. Zhang, B.H. Lu, H.L. Ni, Solvothermal synthesis and thermoelectric properties of lanthanum contained Bi–Te and Bi–Se–Te alloys, Mater. Lett. 59 (2005) 682–685, https://doi.org/10.1016/j.matlet.2004.11.008.

[22] F. Wu, H.Z. Song, J.F. Jia, F. Gao, Y.J. Zhang, X. Hu, Thermoelectric properties of Ce-doped *n*-type $Ce_xBi_{2-x}Te_{2.7}Se_{0.3}$ nanocomposites, Phys. Status Solidi 210 (2013) 1183–1189, https://doi.org/10.1002/pssa.201228589.

[23] W.Y. Shi, F. Wu, K.L. Wang, J.J. Yang, H.Z. Song, X.J. Hu, Preparation and thermoelectric properties of yttrium-doped Bi_2Te_3 flower-like nanopowders, J. Electron. Mater. 43 (2014) 3162–3168, https://doi.org/10.1007/s11664-014-3220-4.

[24] X.B. Zhao, Y.H. Zhang, X.H. Ji, Solvothermal synthesis of nano-sized $La_xBi(2-x)Te3$ thermoelectric powders, Inorg. Chem. Commun. 7 (2004) 386–388, https://doi.org/10.1016/j.inoche.2003.12.020.

[25] O. Ivanov, M. Yaprintsev, R. Lyubushkin, O. Soklakova, Enhancement of thermoelectric efficiency in Bi_2Te_3 via rare earth element doping, Scripta Mater. 146 (2018) 91–94, https://doi.org/10.1016/j.scriptamat.2017.11.031.

[26] M. Yaprintsev, R. Lyubushkin, O. Soklakova, O. Ivanov, Effects of Lu and Tm doping on thermoelectric properties of Bi_2Te_3, J. Electron. Mater. 47 (2018) 1362–1370, https://doi.org/10.1007/s11664-017-5940-8.

[27] O. Ivanov, M. Yaprintsev, Mechanisms of thermoelectric efficiency enhancement in Lu-doped Bi_2Te_3, 015905, Mater. Res. Express 5 (2018) 1–10, https://doi.org/10.1088/2053-1591/aaa265.

[28] M. Yaprintsev, O. Ivanov, A. Vasil'ev, M. Zhezhu, E. Yaprintseva, Effect of Sm-doping on microstructure and thermoelectric properties of textured *n*-type $Bi_2Te_{2.7}Se_{0.3}$ compound due to change in ionic bonding fraction, 122047, J. Solid State Chem. 297 (2021) 1–9, https://doi.org/10.1016/j.jssc.2021.122047 R.

[29] Q.G. Zhang, X. Zhang, B.Y. Cao, M. Fujii, K. Takahashi, T. Ikuta, Influence of grain boundary scattering on the electrical properties of platinum nanofilms, 114102, Appl. Phys. Lett. 89 (2006) 1–3, https://doi.org/10.1063/1.2338885.

[30] H. Zeng, Y. Wu, J. Zhang, C. Kuang, M. Yue, S. Zhou, Grain size-dependent electrical resistivity of bulk nanocrystalline Gd metals, Prog. Nat. Sci. Mater. Int. 23 (2013) 18–22, https://doi.org/10.1016/j.pnsc.2013.01.003.

[31] S. Riedel, J. Röber, T. Geßner, Electrical properties of copper films produced by MOCVD, Microelectron. Eng. 33 (1997) 165–172, https://doi.org/10.1016/S0167-9317(96)00042-1.

[32] O. Ivanov, O. Maradudina, R. Lyubushkin, Grain size effect on electrical resistivity of bulk nanograined Bi_2Te_3 material, Mater. Char. 99 (2015) 175–179, https:doi.org/10.1016/j.matchar.2014.12.001.

[33] O. Ivanov, M. Yaprintsev, A. Vasil'ev, Anisotropy of the grain size effect on the electrical resistivity of *n*-type $Bi_{1.9}Gd_{0.1}Te_3$ thermoelectric textured by spark plasma sintering, J. Eur. Ceram. Soc. 20 (2020) 3431–3436, https://doi.org/10.1016/j.jeurceramsoc.2020.03.048.

[34] M.G. Kanatzidis, Nanostructured thermoelectrics: the new paradigm, Chem. Mater. 22 (2009) 648–659, https://doi.org/10.1021/cm902195j.

[35] M. Takashiri, K. Miyazaki, S. Tanaka, J. Kurosaki, D. Nagai, H. Tsukamoto, Effect of grain size on thermoelectric properties of *n*-type nanocrystalline bismuth-telluride based thin films, 084302, J. Appl. Phys. 104 (2008) 1–6, https://doi:10.1063/1.2990774.

[36] H.J. Goldsmid, Bismuth telluride and its alloys as materials for thermoelectric generation, Mater 7 (2014) 2577–2592, https://doi.org/10.3390/ma7042577.

[37] H. Scherrer, S. Scherrer, Thermoelectrics Handbook: Macro to Nano, CRC Taylor and Francis, Boca Raton, 2012.

[38] S.D. Bhame, D. Pravarthana, W. Prellier, J.G. Noudem, Enhanced thermoelectric performance in spark plasma textured bulk *n*-type $Bi_2Te_{2.7}Se_{0.3}$ and *p*-type $Bi_{0.5}Sb_{1.5}Te_3$, 2190, Appl. Phys. Lett. 102 (2013) 1–3, https://doi.org/10.1063/1.4807771.

[39] X.A. Fan, J.Y. Yang, R.G. Chen, H.S. Yun, W. Zhu, S.Q. Bao, X.K. Duan, Characterization and thermoelectric properties of *p*-type $25\%Bi_2Te_3$–$75\%Sb_2Te_3$ prepared via mechanical alloying and plasma activated sintering, J. Phys. D Appl. Phys. 39 (2006) 740–745, https://doi.org/10.1088/0022-3727/39/4/021.

[40] J. Jiang, L. Chen, S. Bai, Q. Yao, Q. Wang, Fabrication and thermoelectric performance of textured *n*-type $Bi_2(Te,Se)_3$ by spark plasma sintering, Mater. Sci. Eng. B 117 (2005) 334–338, https://doi.org/10.1016/j.mseb.2005.01.002.

[41] Q. Lognon, F. Gascoin, O.I. Lebedev, L. Lutterotti, S. Gascoin, D. Chateigner, Quantitative texture analysis of spark plasma textured *n*-Bi_2Te_3, J. Am. Ceram. Soc. 97 (2014) 2038–2045, https://doi.org/10.1111/jace.12970.

[42] A. Vasil'ev, M. Yaprintsev, O. Ivanov, E. Danshina, Anisotropic thermoelectric properties of $Bi_{1.9}Lu_{0.1}Te_{2.7}Se_{0.3}$ textured via spark plasma sintering, Solid State Sci. 84 (2018) 28–43, https://doi.org/10.1016/j.solidstatesciences.2018.08.004.

[43] Y. Morisaki, H. Araki, H. Kitagawa, M. Orihashi, K. Hasezaki, K. Kimura, Bi_2Te_3-related thermoelectric samples with aligned-texture prepared by plastic deformation, Mater. Trans. 46 (2005) 2518–2524, https://doi.org/10.2320/matertrans.46.2518.

[44] M. Yaprintsev, A. Vasil'ev, O. Ivanov, Thermoelectric properties of the textured $Bi_{1.9}Gd_{0.1}Te_3$ compounds spark-plasma-sintered at various temperatures, J. Eur. Ceram. Soc. 40 (2020) 742–750, https://doi.org/10.1016/j.jeurceramsoc.2019.11.028.

[45] O. Ben-Yehuda, R. Shuker, Y. Gelbstein, Z. Dashevsky, M.P. Dariel, Highly textured Bi_2Te_3-based materials for thermoelectric energy conversion, 113707, J. Appl. Phys. 101 (2007) 1–6, https://doi.org/10.1063/1.2743816.

[46] J.J. Shen, L.P. Hu, T.J. Zhu, X.B. Zhao, The texture related anisotropy of thermoelectric properties in bismuth telluride based polycrystalline alloys, 124102, Appl. Phys. Lett. 99 (2011) 1–3, https://doi.org/10.1063/1.3643051.

[47] F.J. Humphreys, M. Hatherly, Recrystallization and Related Annealing Phenomena, Elsevier, Oxford, UK, 2004.

[48] J.R. Drabble, C.H.L. Goodman, Chemical bonding in bismuth telluride, J. Phys. Chem. Solid. 5 (1958) 142–144, https://doi.org/10.1016/0022-3697(58)90139-2.

[49] S. Nakajima, The crystal structure of $Bi_2Te_{3-x}Se_x$, J. Phys. Chem. Solid. 24 (1963) 479–485, https://doi.org/10.1016/0022-3697(63)90207-5.

[50] X.B. Zhao, X.H. Ji, Y.H. Zhang, G.S. Cao, J.P. Tu, Hydrothermal synthesis and microstructure investigation of nanostructured bismuth telluride powder, Appl. Phys. A 80 (2005) 1567–1571, https://doi.org/10.1007/s00339-004-2956-8.

[51] R.T. Sanderson, Electronegativity and bond energy, J. Am. Chem. Soc. 105 (1983) 2259–2261. https://doi:10.1021/ja00346a026.

[52] G.D. Sproul, Evaluation of electronegativity scales, ACS Omega 5 (2020) 11585–11594, https://doi.org/10.1021/acsomega.0c00831.

[53] M.N. Joswiak, M.F. Doherty, B. Peters, Ion dissolution mechanism and kinetics at kink sites on NaCl surfaces, Proc. Natl. Acad. Sci. Unit. States Am. 115 (2018) 656–661, https://doi.org/10.1073/pnas.1713452115.

[54] L.J. Wang, J.W. Lu, F.S. Xu, F.S. Zhang, Dynamics of crystallization and dissolution of calcium orthophosphates at the near-molecular level, Chin. Sci. Bull. 56 (2011) 713–721, https://doi.org/10.1007/s11434-010-4184-2.

[55] M. Kowacz, M. Prieto, A. Putnis, Kinetics of crystal nucleation in ionic solutions: electrostatics and hydration forces, Geochem. Cosmochim. Acta 74 (2010) 469–481, https://doi.org/10.1016/j.gca.2009.10.028.

[56] A. Baldan, Review progress in Ostwald ripening theories and their applications in γ'-precipitates in nickel base superalloys, Part II Nickel superalloys, J. Mater. Sci 37 (2002) 2379–2405, https://doi.org/10.1023/A:1015408116016.

[57] D.G. Pacheco-Salazara, F.F.H. Aragóna, L. Villegas-Lelovskyc, A. Ortiz de Zevallose, G.E. Marquesd, J.A.H. Coaquira, Engineering of the band gap induced by Ce surface enrichment in Ce-doped SnO_2 nanocrystals, 146794, Appl. Surf. Sci. 527 (2020) 1–7, https://doi.org/10.1016/j.apsusc.2020.146794.

[58] Y.Q. Jia, Crystal radii and effective ionic radii of the rare earth ions, J. Solid State Chem. 95 (1991) 184–187, https://doi.org/10.1016/0022-4596(91)90388-X.

[59] O. Ivanov, M. Yaprintsev, A. Vasil'ev, Comparative analysis of the thermoelectric properties of the non-textured and textured Bi1.9Gd0.1Te3 compounds, 121559, J. Solid State Chem. 290 (2020) 1–10, https://doi.org/10.1016/j.jssc.2020.121559.

[60] J. Burke, D. Turnbull, Recrystallization and grain growth, Prog. Met. Phys. 3 (1952) 220–292, https://doi.org/10.1016/0502-8205(52)90009-9.

[61] F.K. Lotgering, Topotactical reactions with ferrimagnetic oxides having hexagonal crystal structures—I, J. Inorg. Nucl. Chem. 9 (1959) 113–123, https://doi.org/10.1016/0022-1902(59)80070-1.

[62] F. Wu, H. Song, J. Jia, X. Hu, Effects of Ce, Y, and Sm doping on the thermoelectric properties of Bi_2Te_3 alloy, Prog. Nat. Sci. Mater. Int. 23 (2013) 408–412, https://doi.org/10.1016/j.pnsc.2013.06.007.

[63] M. Yaprintsev, A. Vasil'ev, O. Ivanov, Preparation and characterization of nonstoichiometric Te-deficient and Te-rich thermoelectric $Bi_{2-x}Gd_xTe_{3\pm y}$ compounds, 163516, J. Alloys Compd. 900 (2020) 1–9, https://doi.org/10.1016/j.jallcom.2021.163516.